

Towards reconciling experimental and computational determinations of Earth's core thermal conductivity

Monica Pozzo¹, Chris Davies², Dario Alfè^{1,3}

¹*Department of Earth Sciences, London Centre for Nanotechnology and Thomas Young Centre@UCL, University College London, Gower Street, London WC1E 6BT, United Kingdom*

²*School of Earth and Environment, University of Leeds, Leeds LS2 9JT, UK*

³*Dipartimento di Fisica Ettore Pancini, Università di Napoli Federico II, Monte S. Angelo, I-80126, Napoli, Italy*

Abstract

The thermal conductivity (κ) of Earth's core is a critical parameter that controls predictions of core cooling rate, inner core age and the power available to the geodynamo. However, the values of core thermal conductivity inferred from recent studies span a wide range due to the challenges of extrapolating to the pressure-temperature-composition (P-T-C) conditions of the core liquid. In particular, extrapolations of κ from direct experimental determinations are lower than ab initio calculations conducted at core conditions. We have performed density functional theory (DFT) calculations to determine the thermal conductivity and resistivity (ρ) of solid FeSi alloys with two compositions, 4 mol % and 15 mol % Si, at a range of temperatures (850-4350 K) and pressures (60-144 GPa) for ease of comparison with recent directly measured κ values. In agreement with recent experiments, our calculations show that for the larger Si composition the resistivity of the mixture increases substantially, compared to pure Fe, reaching its saturated value already at the lowest temperature investigated. As a result, the thermal conductivity of the mixture is also correspondingly reduced. We also analysed the effect of possible errors in the DFT

Email address: m.pozzo@ucl.ac.uk (Monica Pozzo¹)

calculations due to the neglect of electron-electron scattering (EES) processes. Our results show that experimental and EES-corrected DFT calculations of κ are actually consistent within uncertainties when compared directly at overlapping P-T-C conditions. We present new core thermal history models using our EES-corrected estimates of $\kappa = 75 - 81 \text{ W m}^{-1} \text{ K}^{-1}$ at core-mantle boundary (CMB) conditions, which support previous determinations of late inner core formation around 400-700 Myrs ago and an early molten lower mantle.

Keywords: Earth’s core, Ab initio calculations, DFT, Electrical resistivity, Thermal conductivity

1. Introduction

The Earth’s core electrical ($\sigma = \rho^{-1}$) and thermal conductivities are two fundamental parameters for the modelling of the geodynamo and the thermal history of the Earth. The magnetic field is generated by electric currents in the outer core and the value of the electrical conductivity determines the entropy production that is required to sustain these currents against Ohmic dissipation. The currents are generated by convection, which is driven by thermal and/or compositional buoyancy. Thermal convection is possible if the rate of heat transfer by conduction is low enough, which would be the case for low enough thermal conductivity. Using a low assumed value of $\kappa = 28 - 46 \text{ W m}^{-1} \text{ K}^{-1}$ (Stacey and Anderson, 2001; Stacey and Loper, 2007), core evolution models predict that thermal convection driven by slow cooling provided ample power for magnetic field generation prior to inner core formation around 1 Gyr ago (Labrosse, 2001; Nimmo and Alfè, 2007). These models also favour thermally destabilising conditions throughout the core and hence the absence of a thermally stratified layer below the CMB.

New impetus was injected into the field around a decade ago, when a combination of new theoretical (Sha and Cohen, 2011; Pozzo et al., 2012; de Koker et al., 2012; Pozzo et al., 2013; Pozzo et al., 2014; Davies et al., 2015) and experimental studies (Gomi et al., 2013; Ohta et al., 2014; Ohta et al., 2015; Gomi

21 et al., 2016) suggested much higher thermal conductivity values of $100 - 240 \text{ W}$
22 $\text{m}^{-1} \text{ K}^{-1}$, from CMB to inner-core-boundary (ICB) conditions. Gomi et al.
23 (2013) were the first to point out the well known *saturation* mechanism for the
24 reduced resistivity at high temperature, whereby this stops increasing when the
25 scattering length reaches a value of the order of the atomic distances, the so
26 called Mott-Ioffe-Regel limit (Ioffe and Regel, 1960). This mechanism was also
27 later supported by DFT calculations (Pozzo and Alfè, 2016a). Using these high
28 κ values, core evolution models predicted striking differences from previous re-
29 sults. They showed that maintaining the dynamo for 3.5 Gyrs required much
30 faster cooling rates, a young inner core of only 0.5 Gyrs, and early core tem-
31 peratures far exceeding current estimates of the lower mantle solidus (Davies,
32 2015; Labrosse, 2015; Nimmo, 2015). Additionally, the higher κ values favour
33 thermal stratification at the top of the core (Gomi et al., 2013; Davies et al.,
34 2015).

35 Recently, Davies and Greenwood (2022) have estimated a range of $70 -$
36 $110 \text{ W m}^{-1} \text{ K}^{-1}$ for κ for various Fe-O-Si mixtures at CMB conditions based
37 on consistent extrapolation from a number of recent studies. A thorough review
38 of ρ measurements and calculations of Fe and FeSi alloys at Earth’s and other
39 planetary cores conditions has also been recently published by Berrada and
40 Secco (2021). They point out some discrepancies in the electrical resistivity
41 values between theoretical and experimental studies, which may be ascribed to
42 inconsistencies in measurements and modelling due to different techniques being
43 used, together with a range of pressures and temperatures values attributed to
44 planetary cores. They also find that values of Fe-alloys at Earth’s CMB and
45 ICB do not seem to significantly deviate from that of pure Fe.

46 The drastic changes to the standard model of core evolution implied by high
47 thermal conductivity have driven numerous investigations, including analysis of
48 the paleomagnetic record for signs of inner core formation (Biggin et al., 2015;
49 Bono et al., 2019) and the proposal of new compositional buoyancy sources to
50 alleviate the high cooling rates preceding inner core formation (O’Rourke and
51 Stevenson, 2016; Badro et al., 2016; Hirose et al., 2017; Mittal et al., 2020).

52 Numerous studies have also sought to determine thermal conductivity of iron
53 alloys over a wide range of P-T-C conditions; however, this effort has led to
54 divergent results. A key issue is whether the apparent disagreement reflects
55 differences in 1) experimental vs computational approaches; 2) assumptions
56 regarding extrapolation to core conditions.

57 Here we address this issue by calculating κ and ρ of iron alloys at P-T-C
58 conditions used in recent experimental studies, which permits direct compar-
59 ison between these two complementary approaches. This is crucial, since al-
60 though theoretical and experimental findings agree with high values of σ for the
61 Earth’s core, such an agreement has not yet been reached for κ . In particular,
62 Konôpková et al. (2016) inferred a low thermal conductivity value of 33 W m^{-1}
63 K^{-1} at CMB conditions: this value was derived from a model that used direct
64 measurements of κ at 112 GPa at various temperatures, and included resistivity
65 data at room T extrapolated to 112 GPa and also shock wave resistivity data
66 interpolated to 112 GPa, which were all converted to κ using the Wiedemann-
67 Franz law $\kappa = \sigma LT$ (where T is the temperature) and a value of 1.9×10^{-8}
68 $\text{W } \Omega \text{ K}^{-2}$ for the Lorenz parameter L . This result was in stark disagreement
69 with the value of $\kappa = 90 \text{ W m}^{-1} \text{ K}^{-1}$ found by Ohta et al. (2016), from their
70 ρ measurements, taking account of resistivity saturation and the Wiedemann-
71 Franz law with an ideal value $L_0 = 2.44 \times 10^{-8} \text{ W } \Omega \text{ K}^{-2}$. To reconcile the
72 two sets of measurements would require using in the Ohta et al. (2016) data a
73 value of L to be one third of L_0 , which is much lower than values obtained by
74 direct calculation (de Koker et al. 2012; Pozzo et al. 2012, 2013, 2014; Pozzo
75 and Alfè, 2016b; Secco, 2017; Pourovskii, 2020) and which would also need to
76 have a strong pressure and temperature dependence. Indeed, Konôpková et
77 al. (2016) noted that their minimum measured thermal conductivity did not
78 include saturation (on the basis that resistivity saturation in Fe at extreme PT
79 conditions was not clearly confirmed by theoretical studies and because avail-
80 able saturation models could not satisfactorily describe the data). However,
81 they pointed out that if they assumed that resistivity saturation had occurred,
82 then thermal conductivities at core conditions would be somewhat higher, 60-80

83 $\text{W m}^{-1} \text{K}^{-1}$, than obtained from their modelling.

84 More recently, Zhang et al. (2020) reported new measurements of σ and
85 κ of hcp iron up to pressures of 180 GPa and temperatures of 4000 K. Their
86 results fall somewhat in the middle between those of Konôpková et al. (2016)
87 and Ohta et al. (2016). They also report values of the Lorenz parameter
88 between 2.0 and $2.3 \times 10^{-8} \text{ W } \Omega \text{ K}^{-2}$, which are somewhat lower than L_0 but
89 show no dramatic pressure and/or temperature dependence. Additional recent
90 experiments by Hsieh et al. (2021) were performed on pure iron at ambient
91 temperature, and on $\text{Fe}_{0.96}\text{Si}_{0.04}$ and $\text{Fe}_{0.85}\text{Si}_{0.15}$ mixtures, both at ambient and
92 at temperatures up to 3300 K. For pure iron at ambient temperature, κ values
93 of up to $120 \text{ W m}^{-1} \text{K}^{-1}$ were reported at pressures of 120 GPa, while for the
94 mixtures the thermal conductivities were much reduced. At higher than ambient
95 temperatures the thermal conductivities of the mixtures increased compared to
96 the room temperature values, as expected, and it is expected that also those of
97 pure iron would increase correspondingly, even though Hsieh et al. (2021) argue
98 (without measuring them) that they would decrease, to the point of being in
99 agreement with the low values of $\simeq 33 \text{ W m}^{-1} \text{K}^{-1}$ measured by Konôpková
100 et al. (2016). For this to happen, the Lorenz number would have to show a
101 strong decrease with temperature, because ρ increases at most linearly with
102 temperature (and less than linearly once saturation starts to have an effect),
103 which is incompatible with the values of the Lorenz parameter of $2.0\text{-}2.3 \times 10^{-8}$
104 $\text{W } \Omega \text{ K}^{-2}$ reported by Zhang et al. (2020). In fact, departure from L_0 has been
105 noted for both pure iron and iron alloys in previous theoretical calculations (de
106 Koker et al., 2012; Pozzo et al., 2012; Pozzo et al. 13; Pozzo et al., 2014; Pozzo
107 and Alfè, 2016b; Pourovskii et al., 2020). These show that the Wiedemann-
108 Franz law strongly depends on temperature and alloy composition, providing
109 Lorenz number values ranging from 1.6 to $2.8 \times 10^{-8} \text{ W } \Omega \text{ K}^{-2}$, but these
110 values are still far too large to reconcile the very low thermal conductivity
111 values reported in Konôpková et al. (2016).

112 On the theoretical side, it has been pointed out that one possible prob-
113 lem with DFT calculations is the incomplete treatment of the electron-electron

114 scattering (EES) mechanism. This was initially addressed by Pourovskii et al.
 115 (2017), who published new results obtained with post DFT methods based on
 116 dynamical mean field theory (DMFT) techniques. By taking into account both
 117 EES and electron-lattice scattering (ELS), they found $\kappa = 190 \text{ W m}^{-1} \text{ K}^{-1}$
 118 at Earth's inner core (IC) conditions and a Lorenz parameter $L = 2.04 \times 10^{-8}$
 119 $\text{W } \Omega \text{ K}^{-2}$, which is lower than L_0 , but still much higher than what would be
 120 required to reconcile the experimental value of $\sim 50 \text{ W m}^{-1} \text{ K}^{-1}$ inferred from
 121 measurements by Konôpková et al. (2016) at IC conditions. A similar theoret-
 122 ical approach, also based on DMFT, was used by Xu et al. (2018), who obtained
 123 $\kappa = 150 \text{ W m}^{-1} \text{ K}^{-1}$ at similar conditions. The DMFT based reported values of
 124 κ were substantially lower than the DFT value (about $240 \text{ W m}^{-1} \text{ K}^{-1}$; Pozzo
 125 et al., 2014), suggesting a sizeable contribution of the EES mechanism, however,
 126 those calculations were performed on a perfect Fe crystal. Since EES depends on
 127 the value of the electron density of states at the Fermi energy, and since this is
 128 significantly affected by thermal disorder, it is expected that the contribution of
 129 EES to the thermal and electrical conductivities would also be significantly af-
 130 fected by thermal disorder, an effect which was not included in Pourovskii et al.
 131 (2017) and Xu et al. (2018), although the latter did report preliminary results
 132 for snapshots of a system representing the liquid and found that EES increases
 133 with thermal disorder. Hausoel et al. (2017) studied face-centred-cubic Ni at
 134 Earth's core conditions, and found that thermal disorder did not affect correla-
 135 tion much. The work of Zhang et al. (2020) mentioned above also included a
 136 theoretical study of ρ of hcp Fe. Calculations were performed either including
 137 only the ELS term, or both ELS and EES (ELS+EES), showing that the two
 138 sets of results are close at low temperature, but deviate significantly from each
 139 other as temperature is increased. The calculations were again performed on
 140 the perfect hcp crystal, however, the authors also reported one ELS+EES cal-
 141 culation at $T = 2000 \text{ K}$ performed on snapshots of the solid including thermal
 142 disorder (ELS+EES+TS). At this temperature the difference between the ELS
 143 and the ELS+EES calculations is small, but the ELS+EES+TS result appear to
 144 be closer to the ELS one than to the ELS+EES, again suggesting that thermal

145 disorder moderates the inclusion of EES substantially.

146 More recently, some of us have re-visited the electronic correlations and
147 transport in pure iron at Earth’s core conditions (Pourovskii, 2020) using DMFT.
148 We studied both the hexagonal-closed-packed(hcp) and the body-centred-cubic(bcc)
149 structures at 330 GPa and 5800 K, and found that the inclusion of EES lowers
150 κ , but we also found that once thermal disorder is introduced this reduction
151 is at most 24%, a much more moderate effect compared to the case in which
152 calculations are performed on the perfect crystal. By contrast, ρ is much less
153 affected by the inclusion of EES, increasing by only 9% over the ELS value.

154 Here we have extended our previous calculations on ρ of hcp Fe reported
155 in Pozzo and Alfè (2016a, 2016b) by including κ values, and we have also per-
156 formed calculations at similar pressure/temperature conditions on the two mix-
157 tures $\text{Fe}_{0.96}\text{Si}_{0.04}$ and $\text{Fe}_{0.85}\text{Si}_{0.15}$, which allow a more direct comparison with
158 the most recent experiments of Hsieh et al. (2021) and Inoue et al. (2020).
159 The calculations have been performed using DFT and the Kubo-Greenwood
160 approach (Kubo, 1957; Greenwood, 1958) for ρ and the Chester-Thellung-Kubo-
161 Greenwood approach (Chester and Thellung, 1961) for the electronic contribu-
162 tion to κ . The ionic contribution to κ is expected to be small and, as in previous
163 studies, it has been neglected - it might increase the total thermal conductivity
164 by only 2.5 to 4 $\text{W m}^{-1} \text{K}^{-1}$, depending on pressure/temperature conditions
165 (Pozzo et al., 2012). Once the possible overestimation of κ due to the inclusion
166 of only the ELS term is taken into account, we find that our results are com-
167 patible with the experimental measurements. Our calculations also confirm the
168 remarkable reduction of thermal conductivity of the mixtures compared to that
169 of pure iron, found in the experimental data (Hsieh et al., 2021), especially for
170 the mixture with the larger amount of silicon.

171 2. Techniques

172 All the DFT calculations for this work were performed by using similar tech-
173 niques to those used in our previous papers (Alfè et al., 2012; Pozzo et al., 2012,
174 2013, 2014; Pozzo and Alfè, 2016a, 2016b). The VASP code simulation package

175 (Kresse and Furthmuller, 1996) was used with the projector augmented wave
176 (PAW) method (Blöchl, 1994; Kresse and Joubert, 1999), together with the
177 Perdew-Wang (Wang and Perdew, 1991) functional (PW91). We used PAW
178 potentials with [Ne]3s² and [Ne] core for iron and silicon, and respective valence
179 configurations 3p⁶4s¹3d⁷ and 3s²3p², with core radii of 1.16 Å and 0.79 Å. A
180 plane-wave basis set was used to expand the electronic wave-functions with an
181 energy cutoff of 380 eV. Electronic levels were occupied according to Fermi-Dirac
182 statistics. Configurations in the canonical ensemble were generated by running
183 molecular dynamics (MD) simulations, in which temperature was controlled by
184 a combination of a Nosé (Nosé, 1984) and an Andersen (Andersen, 1980) ther-
185 mostat, using a time step of 1 fs and using the Γ point only to sample the
186 Brillouin zone. An efficient charge density extrapolation was used to speed up
187 the MD simulations (Alfè, 1999), which we typically ran for 9-12 ps, discarded
188 the first ps to allow for equilibration, and extracted typically 30-40 configura-
189 tions equally spaced in time on which we computed the electrical and thermal
190 conductivities, using 2 \mathbf{k} -points to sample the Brillouin zone. The electrical
191 conductivity was computed using the Kubo-Greenwood (Kubo, 1957; Green-
192 wood, 1958) formula and the thermal conductivity using the Chester-Thellung-
193 Kubo-Greenwood (Chester and Thellung, 1961) formula, as implemented in
194 VASP by Desjarlais (Desjarlais et al. 2002). Lorenz parameters were obtained
195 as $L = \kappa/\sigma T$.

196 The calculations were performed on supercells containing 490 atoms, with
197 total of 20 and 74 Fe atoms randomly substituted with Si atoms to obtain 4
198 % and 15 % alloying compositions. For the 15 mol % alloying composition,
199 we also checked convergence of the electrical and thermal conductivities with
200 respect to the size of the simulation supercell for the lowest temperature of
201 850 K. This was done by performing additional calculations with two supercells
202 including 768 and 972 atoms in which we substituted 115 and 146 Fe atoms with
203 Si respectively. We also checked that in all our simulations the system under
204 scrutiny remained solid throughout.

205 **3. Results**

206 In Table 1 we report ρ data of pure solid iron as computed earlier (Pozzo
207 and Alfè, 2016a), also including κ data and the Lorenz parameter L (Pozzo and
208 Alfè, 2016b). In Tables 2 and 3 we report ρ and κ data computed in this work
209 for hcp iron with 4% and 15% Si respectively (where compositions are given in
210 mol %).

211 The resistivity data for the three systems are also plotted in Fig. 1. We
212 report our raw DFT data, as well as these data increased by 9%, which is the
213 likely correction due to lack of the EES contribution missing in our calculations,
214 as quantified in Pourovskii et al. (2020). Perhaps the most striking feature in
215 Fig. 1 is the large increase in the resistivity of the 15% Si mixture compared
216 with that of pure iron, and also compared with that of the system with 4% Si.
217 Interestingly, the resistivity of the 15% Si mixture is also almost independent on
218 temperature and rather shows a small negative temperature dependence. This
219 trend was observed at much lower and constant pressures in the solid state of
220 high silicon Fe-Si alloys by Baum et al. (1967) at 1 atm, and also in recent work
221 by Berrada et al. (2020) on solid Fe8.5wt%Si and increasingly so on Fe17wt%Si
222 at pressures in a 3-5 GPa range. It was also reported for solid and lower silicon
223 Fe4.5wt%Si by Silber et al. (2019) at pressures in a 3-9 GPa range.

224 As previously highlighted (Pozzo et al., 2011), large resistivities calculated
225 within the Kubo-Greenwood approach may be an artefact of the size of the
226 simulation cell, which must be large enough to accommodate the length of the
227 mean free path. For instance, we found that in liquid Na at ambient conditions
228 we needed to use simulation cells including at least 1000 atoms to obtain a
229 converged resistivity. This potential problem is of course more likely to appear
230 at low temperature, where the mean free paths are longer. For this reason,
231 in addition to the simulation performed with a 490-atom cell, we repeated the
232 calculation for the 15% Si mixture at 850 K using 768- and 972-atom cells. The
233 electrical and thermal conductivities computed with these larger cells were in-
234 distinguishable from those obtained with the smaller 490-atom cells, indicating

T	P	ρ	κ	L
K	GPa	($10^{-6}\Omega\text{ m}$)	($\text{W m}^{-1}\text{ K}^{-1}$)	($10^{-8}\text{ W }\Omega\text{ K}^{-2}$)
4350	97	0.716(2)	171(1)	2.81
3350	85	0.653(3)	141(1)	2.75
2350	73	0.527(4)	114(1)	2.56
1850	68	0.424(3)	105(1)	2.41
1350	63	0.321(3)	99(1)	2.35
850	59	0.200(2)	100(1)	2.35

Table 1: Temperature (T), pressure (P), resistivity (ρ), thermal conductivity (κ) and Lorenz parameter (L) for pure solid iron from Pozzo and Alfè (2016a, 2016b).

T	P	ρ	κ	L
K	GPa	($10^{-6}\Omega\text{ m}$)	($\text{W m}^{-1}\text{ K}^{-1}$)	($10^{-8}\text{ W }\Omega\text{ K}^{-2}$)
4350	99	0.766(2)	154.3(5)	2.72
3350	86	0.730(2)	125.7(3)	2.74
2350	75	0.660(2)	93.4(2)	2.62
2050	72	0.626(2)	84.5(3)	2.58
1850	70	0.605(2)	77.5(3)	2.53
1350	65	0.529(2)	62.3(2)	2.44
850	61	0.455(2)	44.2(1)	2.36

Table 2: Temperature (T), pressure (P), resistivity (ρ), thermal conductivity (κ) and Lorenz parameter (L) for $\text{Fe}_{0.96}\text{Si}_{0.04}$ solid (composition is given in mol %).

235 that the large resistivity found for this system is a real effect. The apparent
236 temperature independence of this resistivity also indicates that the determina-
237 tion of the mean free path is dominated by the presence of the Si impurities
238 rather than by temperature.

239 Experimental values for two similar Si composition mixtures (2 and 6.5 wt
240 %, corresponding to 4 and 12 mol %) from Inoue et al. (2020) are also plotted
241 in Fig. 1. The lower temperature experimental point for the 4% Si mixture
242 (44 GPa, 1340 K) is in agreement with our corrected computed value (65 GPa,
243 1350 K), and the small difference in pressure between the two set of data is
244 not expected to affect the value of the resistivity appreciably (Secco, private
245 communication).

246 Thermal conductivities for the 4% and 15% Si mixtures are plotted in Figs. 2
247 and 3. We report our raw DFT data, as well as these data reduced by 24%,
248 which is the likely correction due to lack of the EES contribution missing in

T	P	ρ	κ	L
K	GPa	($10^{-6}\Omega\text{ m}$)	($\text{W m}^{-1}\text{ K}^{-1}$)	($10^{-8}\text{ W }\Omega\text{ K}^{-2}$)
4350	103	0.928(2)	120.2(2)	2.56
3350	92	0.930(2)	95.0(2)	2.64
3000	144	0.883(2)	90.5(2)	2.66
3000	106	0.916(2)	87.1(2)	2.66
2500	106	0.917(2)	72.1(2)	2.65
2350	81	0.946(2)	65.5(1)	2.64
2200	79	0.947(2)	61.4(1)	2.64
1850	76	0.951(2)	50.0(1)	2.57
1350	72	0.965(2)	35.4(1)	2.53
850	67	0.967(2)	21.5(1)	2.45

Table 3: Temperature (T), pressure (P), resistivity (ρ), thermal conductivity (κ) and Lorenz parameter (L) for $\text{Fe}_{0.85}\text{Si}_{0.15}$ solid (composition is given in mol %).

our calculations. In both figures we also report the experimental data of Hsieh et al. (2021). They note that temperature values are average measurement temperatures. They do not provide an uncertainty value, but from the caption of their Supplementary Table 5 we can infer that it is likely to be of the order of 550 K. In the case of $\text{Fe}_{0.96}\text{Si}_{0.04}$, Hsieh et al. (2021) report values of κ at different pressures but at the same temperature of 2050 K. From Fig. 2 it is clear that our calculated κ at 2050 K and 72 GPa is higher than the corresponding experimental value (2050 K and 70 GPa, blue square), but agreement is reached after taking into account the effect of EES contributions (see dotted line) plus the experimental measurement uncertainties.

Similarly, our calculated values for κ of the $\text{Fe}_{0.85}\text{Si}_{0.15}$ mixture are higher than experimental ones (Hsieh, 2021), as shown in Fig. 3. In this case the two sets of results could be still compatible for at least some of the data (e.g. 2500 and 3000 K at 106 GPa) once the possible EES effect (although as suggested by Zhang et al. (2020) this error should decrease with decreasing temperature) and the experimental measurements uncertainties are taken into account. We also note that the experimental data are quite scattered, indicating the likely size of the error. At high pressure (144 GPa and 3000 K) the experiments report very low thermal conductivity values, which are incompatible with our calculated ones. We note that κ experimental measured values increase for increasing

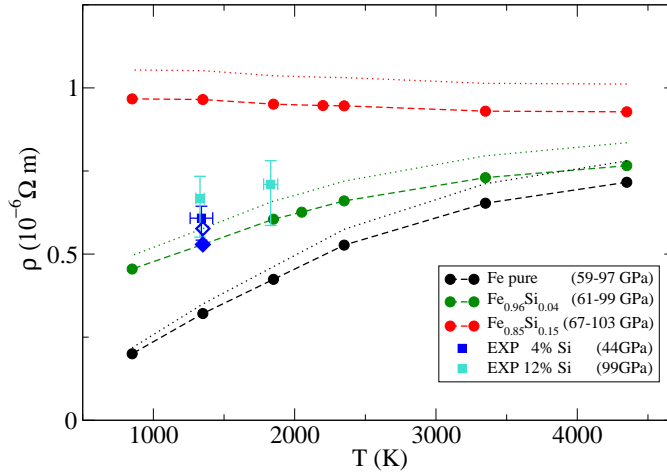


Figure 1: Electrical resistivity (ρ) of pure solid Fe, $\text{Fe}_{0.96}\text{Si}_{0.04}$ and $\text{Fe}_{0.85}\text{Si}_{0.15}$ as a function of temperature (T). Calculations have been performed at constant volumes and so pressures increase with temperature, as indicated in the legend for the respective cases. Also shown present calculations increased by 9% (dotted lines), which is an estimate of the possible error due to absence of EES contributions (see text). Experimental values for similar mixtures from Inoue et al. (2020) are also shown. The blue filled diamond is from present calculations at similar PT as used in experiments (44 GPa, 1340 K); the corresponding computed value increased by 9% is shown as an open diamond (see text for details).

269 temperature at every given pressure as predicted by our computational results
 270 until 106 GPa. At higher pressures, experimental values are not following the
 271 expected behaviour, since they do not increase for increasing temperature values,
 272 making us wonder if this could be due to the presence of (partial) melt in the
 273 experimental samples.

274 Another important aspect to consider is the onset of the saturation effect. As
 275 shown in Fig. 1, the onset of saturation behaviour for $\text{Fe}_{0.96}\text{Si}_{0.04}$ solid is clearly
 276 visible at temperatures above 2500 K. We previously noticed the same effect
 277 for pure solid Fe (Pozzo and Alfè, 2016a). This seems to be in contradiction
 278 with recent findings by Zhang et al. (2020) on the resistivity of solid Fe up to
 279 ~ 3000 K, who point to an apparent almost linear dependence on temperature.
 280 However, from our results (Pozzo and Alfè, 2016a) at the pressure values studied

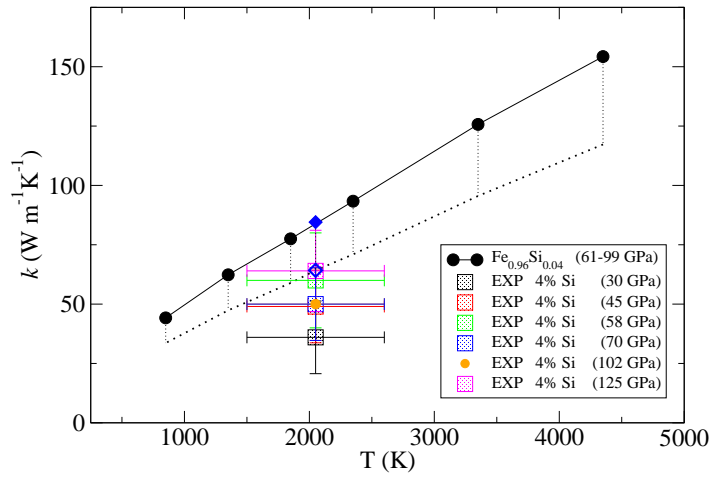


Figure 2: Thermal conductivity of $\text{Fe}_{0.96}\text{Si}_{0.04}$ solid as a function of temperature. Present calculations (black filled circles) cover 61-99 GPa in the 850-4350 K temperature range (see Table 2). Also shown present calculations reduced by 24% (dotted line), which is an estimate of the possible error due to absence of EES contributions (see text). The experimental data for the same mixture from Hsieh et al. (2021) are plotted in different coloured symbols as shown in the inset legend. The blue filled diamond is from present calculations at the same PT experimental conditions (70 GPa, 2050 K); the corresponding computed value reduced by 24% is shown as an open diamond.

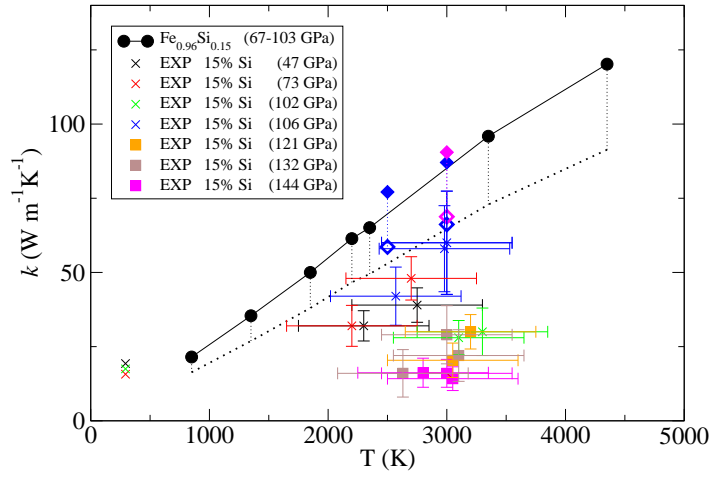


Figure 3: Thermal conductivity of $\text{Fe}_{0.85}\text{Si}_{0.15}$ solid as a function of temperature. Present calculations (black filled circles) cover 67-103 GPa in the 850-4350 K temperature range (see Table 3). Also shown present calculations reduced by 24% (dotted line), which is an estimate of the possible error due to absence of EES contributions (see text). The experimental data for the same mixture from Hsieh et al. (2021) are plotted in different coloured symbols as shown in the inset legend. Filled diamonds are present calculations at the same PT experimental conditions, plotted with corresponding colours; computed values reduced by 24% are shown as open diamonds.

281 by Zhang et al. we would expect the onset of the saturation behaviour to start
282 at about 3600 K, which is well above their maximum experimental working
283 temperature. By contrast, Inoue et al. (2020), despite sampling temperatures
284 up to 3120 K only, were able to detect the onset of the saturation behaviour
285 for hcp Fe-2, 4 and 6.5 wt.% Si. From our $\text{Fe}_{0.96}\text{Si}_{0.04}$ solid results, we can see
286 that in the case of a 4% mixture the onset of the saturation behaviour starts
287 at a lower temperature of about 2500 K and it was indeed detected by Inoue et
288 al. Therefore we argue that the resistivity saturation behaviour in Fe and iron
289 alloys should be easily detected in experimental investigations, providing these
290 sample a temperature range up to large enough values.

291 4. Geophysical implications

292 The results presented in Section 3 show that experimental and theoretical κ
293 values are consistent within uncertainties when compared directly at overlapping
294 P-T-C conditions. Previously, we calculated values of 107, 99 and 101 W m^{-1}
295 K^{-1} at the top of the outer core for Fe-O-Si mixtures along three different
296 adiabatic profiles, at temperatures of 5700, 5500 and 5300K respectively (Pozzo
297 et al., 2013; Davies et al. , 2015). Here we would like to revisit the errors
298 on those values by taking into account a possible 24% correction due to EES
299 contributions. Therefore, we propose to replace our previous values at CMB
300 conditions with a range of values spanning from 107, 99 and 101 $\text{W m}^{-1} \text{K}^{-1}$
301 to 81, 75 and 77 $\text{W m}^{-1} \text{K}^{-1}$ respectively.

302 To investigate the implications of these new κ values for Earth's core we
303 estimate its thermal history using the model described in Davies (2015). Briefly,
304 we integrate the core energy and entropy balances backwards in time for 3.5
305 Gyrs. The energy balance determines the core cooling rate by relating the CMB
306 heat flow Q_{cmb} to the power sources in the core. We do not consider precipitation
307 of oxides (e.g. O'Rourke and Stevenson, 2016; Hirose et al., 2017) because the
308 onset and rate of precipitation are currently poorly constrained (Davies and
309 Greenwood, 2022). Adding precipitation of MgO could increase the predicted
310 inner core age by a factor of 1.1-2 (Davies and Greenwood, 2022). In addition,

311 we omit terms due to compressional heating and heat of reaction since they are
 312 tiny compared to the leading terms (Gubbins et al, 2003; Davies, 2015; Nimmo,
 313 2015). The final energy equation is then a balance between CMB heat flow
 314 and secular cooling, radiogenic heating, latent heat and gravitational energy
 315 release that accompany inner core growth. Dynamo activity is assessed using
 316 the entropy balance, which relates the entropy sources from secular cooling,
 317 radiogenic heating, latent heat and gravitational energy release to the entropy
 318 of thermal conduction (which depends on κ), and the dynamo entropy E_J that
 319 defines the entropy production due to dynamo action.

320 All parameter values except κ are taken from Davies et al. (2015). The
 321 main uncertainty in the calculation is the density jump $\Delta\rho$ at the ICB, which
 322 sets the core composition and melting temperature. We use the three values of
 323 $\Delta\rho = 0.6, 0.8$ and 1.0 gm/cc that span the uncertainties determined from normal
 324 mode studies (Masters and Gubbins, 2003) together with the corresponding
 325 compositions and temperature profiles in Davies et al. (2015). Following Nimmo
 326 (2015) we prescribe Q_{cmb} during the period of inner core growth and the entropy
 327 production E_J prior to inner core formation. This assumption generates a
 328 plausible variation of CMB heat flow with time. We vary the present Q_{cmb}
 329 value such that the model produces an E_J prior to inner core formation that
 330 is marginally positive, which is required to satisfy paleomagnetic predictions of
 331 continuous dynamo activity back to 3.5 Ga (Tarduno et al., 2010; Davies et al.,
 332 2022) and also yields a conservatively low core cooling rate and hence inner core
 333 age and ancient CMB temperature. All models are also required to match the
 334 present ICB radius of 1221 km.

335 Figure 4 shows the predicted inner core age and CMB temperature at 3.5
 336 Gyrs ago for the three values of $\Delta\rho$ and three sets of κ values: an old and low κ
 337 value of $46 \text{ W m}^{-1} \text{ K}^{-1}$ (green symbols) inferred by Stacey and Anderson (2001);
 338 the DFT-only κ values (purple) reported in Pozzo et al. (2013) and Davies et
 339 al. (2015); and the new values (red). We also run models with the addition
 340 of 30 ppm ^{40}K as suggested by Xiong et al. (2018), which confirm that such
 341 a small amount of radiogenic heating has a negligible impact on the results.

342 In all cases higher $\Delta\rho$ increases the inner core age and decreases the ancient
343 CMB temperature because enhanced gravitational power allows the dynamo to
344 operate at lower cooling rate. As expected, the new results sit in-between the
345 two older datasets, with a predicted inner core age of 400-700 Myrs. This range
346 is broadly consistent with previous thermal history models that included high
347 thermal conductivity (e.g. Driscoll and Bercovici, 2014; Labrosse, 2015; Davies
348 et al., 2022). Maintaining the geodynamo with such a young inner core requires
349 a rapid cooling rate over most of Earth’s history, which implies that the core
350 formed hot. All models predict that the ancient CMB temperature far exceeded
351 estimates of the lower mantle solidus, suggesting an early molten lower mantle
352 permitting efficient thermal and chemical exchange with the core (Davies et al.,
353 2020).

354 Our calculations estimate the present-day adiabatic heat flow at the CMB
355 to lie in the range 10-12 TW. Estimates of the total present CMB heat flow
356 range from 7-17 TW (Nimmo, 2015) with recent work favouring $Q_{\text{cmb}} \approx 15$
357 TW (Frost et al, 2022). It is therefore possible that the top of the core is
358 presently sub- or super-adiabatic, though the numbers above favour the former
359 scenario. Nevertheless the sub-adiabatic case is of interest because independent
360 geomagnetic (Buffett, 2012) and seismic (Helffrich and Kaneshima, 2010) ob-
361 servations have been used to infer the presence of a stratified layer atop the
362 core. Sub-adiabatic conditions require the presence of a region below the CMB
363 that is stable to thermal convection, though it may not be stable to convection
364 overall since the destabilising chemical buoyancy arising from inner core growth
365 renders the region susceptible to double-diffusive instabilities. Considering the
366 minimum CMB heat flow of 7 TW, calculations with $k = 70$ W/m/K, similar to
367 our values, estimated the maximum thickness of the thermally stable region to
368 lie in the range 400-500 km (Davies and Greenwood, 2022). The corresponding
369 strength of thermal stratification is, however, too weak to match the model of
370 Helffrich and Kaneshima (2010). This discussion suggests that any stratification
371 in the upper core owes its existence to chemical (rather than thermal) effects,
372 such as incomplete mixing during core formation (Landeau et al, 2017; Bouffard

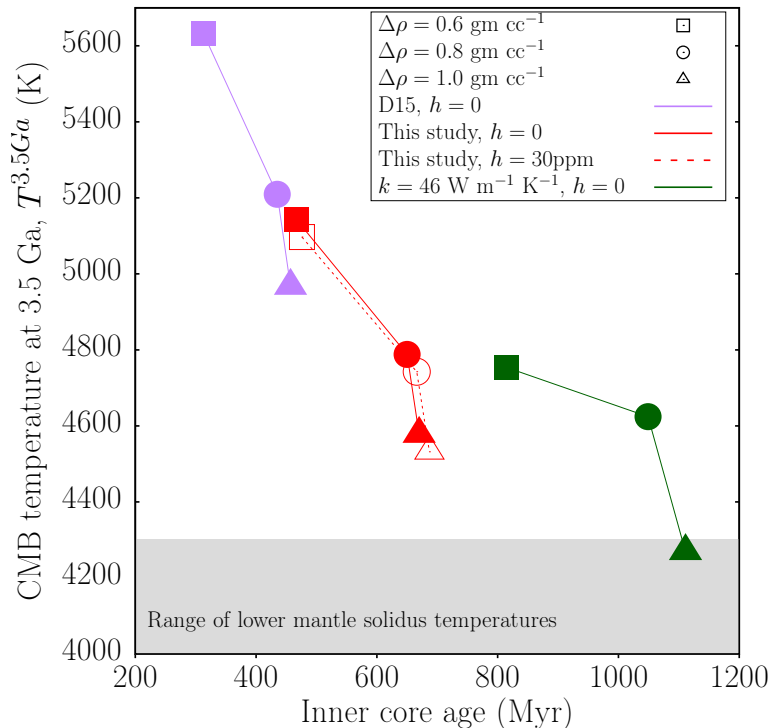


Figure 4: Predicted inner core age and CMB temperature at 3.5 Gyrs ago from thermal history models for $\Delta\rho = 0.6, 0.8$ and 1.0 gm/cc and three sets of κ values: $46 \text{ W m}^{-1} \text{ K}^{-1}$ (green symbols) as inferred by Stacey and Anderson (2001); our previous DFT-only κ values (purple) reported in Pozzo et al. (2013) and Davies et al. (2015); and our new proposed values from this study (red). Data from our current models also including 30 ppm ^{40}K are shown as red open symbols.

373 et al, 2020) or mass exchange with the mantle or basal magma ocean (Buffett
 374 and Seagle, 2010; Davies et al, 2020).

375 5. Conclusions

376 In this paper we have presented new DFT calculations of the thermal con-
 377 ductivities and electrical resistivities of two solid iron alloys, $\text{Fe}_{0.96}\text{Si}_{0.04}$ and
 378 $\text{Fe}_{0.85}\text{Si}_{0.15}$, to replicate experimental determinations made at the same pres-
 379 sure, temperature and alloy concentrations. We see the onset of resistivity
 380 saturation for the 4% mixture, whereas the 15% mixture has already reached
 381 its saturated value at the lowest temperature investigated and the resistivity

382 is almost independent of temperature. We compare our thermal conductivity
383 values with direct measurements available in literature. Our DFT calculations
384 do not include EES contributions, which as shown recently could result in an
385 overestimation of the thermal conductivity of up to $\simeq 24\%$ (Pourovskii et al.,
386 2020).

387 Once both computational and experimental uncertainties are taken into ac-
388 count, we find agreement in κ values for both mixtures for at least some of the
389 data. In particular, for the 4% Si mixture, our corrected κ value of 64 W m^{-1}
390 K^{-1} at 72 GPa and 2050 K agrees with the experimental value of $50 \pm 15 \text{ W}$
391 $\text{m}^{-1} \text{K}^{-1}$ measured by Hsieh et al. (2021) at 70 GPa and 2050 K. For the
392 15% Si mixture, we find a corrected κ value of $66 \text{ W m}^{-1} \text{K}^{-1}$ at 106 GPa and
393 3000 K, which is in very good agreement with the value of $60 \pm 17 \text{ W m}^{-1} \text{K}^{-1}$
394 measured by Hsieh et al. (2021) at the same PT conditions. The comparisons
395 presented in the present work should lend confidence to previously calculated
396 thermal conductivity values at Earth’s core conditions, albeit augmented with
397 a larger error estimate due to possible EES processes. Considering this $\simeq 24\%$
398 reduction in thermal conductivity, our new thermal history models predict a
399 young inner core (400-700 Myrs old) which is still very hot at ancient times,
400 suggesting a basal magma ocean interaction for most of Earth’s history.

401 **Acknowledgements**

402 M.P. and D.A. acknowledge support from the Natural Environment Research
403 Council (NERC) Grant No. NE/R000425/1. C.D. acknowledges a NERC Push-
404 ing the Frontiers award, reference NE/V010867/1. M.P., D.A. and C.D. also
405 acknowledge support from NERC Grant No. NE/T000228/1. Calculations were
406 performed on the U.K. national service Archer, and on the Monsoon2 system,
407 a collaborative facility supplied under the Joint Weather and Climate Research
408 Programme, a strategic partnership between the UK Met Office and NERC.
409 We would like to thank R. Secco and a second anonymous referee for useful
410 suggestions to improve the manuscript.

411 **Declaration of competing interests**

412 The authors declare that they have no competing interests.

- 413 [1] Alfè, D., 1999. Ab initio molecular dynamics, a simple algorithm for charge
414 extrapolation. *Comp. Phys. Comm.* 118, 31-33.
- 415 [2] Alfè, D., Pozzo, M., Desjarlais, M.P., 2012. Lattice electrical resistivity
416 of magnetic bcc iron from first-principles calculations. *Phys. Rev. B* 85,
417 024102, 1-4.
- 418 [3] Andersen, H.C., 1980. Molecular dynamics simulations at constant pressure
419 and/or temperature. *J. Chem. Phys.* 72, 2384-2393.
- 420 [4] Badro, J., Siebert, J., Nimmo, F., 2016. An early geodynamo driven by
421 exsolution of mantle components from Earth's core. *Nature* 536, 326-328.
- 422 [5] Baum, B.A., Gel'd, P.V., Tyagunov, G.V., 1967. Resistivity of ferrosilicon
423 alloys in the temperature range 800-1700 °C. *Phys. Metals and Metallog.*
424 24, 181-184.
- 425 [6] Berrada, M., Secco, R.A., 2021. Review of electrical resistivity measure-
426 ments and calculations of Fe and Fe-alloys relating to planetary cores.
427 *Front. Earth Sci.* 9, 732289, 1-21.
- 428 [7] Berrada, Secco, R.A., Yong, W., Littleton, J.A.H., 2020. Electrical resis-
429 tivity measurements of Fe-Si with implications for the early lunar dynamo.
430 *J. Geophys. Res. Planets* 125, e2020JE006380.
- 431 [8] Biggin, A., Piispa, E., Pesonen, L., Holme, R., Paterson, G., Veikkolainen,
432 T., Tauxe, L., 2015. Palaeomagnetic field intensity variations suggest Meso-
433 proterozoic inner-core nucleation. *Nature* 526, 245-248.
- 434 [9] Blöchl, P.E., 1994. Projector augmented-wave method. *Phys. Rev. B* 50,
435 17953-17979.

- 436 [10] Bono, R.K., Tarduno, J.A., Nimmo, F., Cottrell, R.D., 2019. Young inner
437 core inferred from Ediacaran ultra-low geomagnetic field intensity. *Nat.*
438 *Geosci.* 12 (2), 143-147.
- 439 [11] Bouffard, M., Landeau, M., Goument, A., 2020. Convective erosion of a
440 primordial stratification atop Earth's core. *Geophys. Res. Lett.* 47 (14),
441 e2020GL087109.
- 442 [12] Buffett, B.A., 2012. Geomagnetism under scrutiny. *Nature* 485, 319320.
- 443 [13] Buffett, B.A., Seagle, C.T., 2010. Stratification of the top of the core due
444 to chemical interactions with the mantle. *J. Geophys. Res. Solid Earth* 115,
445 B04407.
- 446 [14] Chester, G.V., Thellung, A., 1961. The Law of Wiedemann and Franz.
447 *Proc. Phys. Soc. London* 77, 1005-1013.
- 448 [15] Davies C., Greenwood, S., 2022. Dynamics in Earth's core arising from
449 thermo-chemical interactions with the mantle. Accepted for publication
450 in the AGU Monograph "core-mantle evolution - a multidisciplinary ap-
451 proach". DOI: <https://doi.org/10.31223/X5MW4G>.
- 452 [16] Davies, C., 2015. Cooling history of Earth's core with high thermal con-
453 ductivity. *Phys. Earth. Planet. Int.* 247, 65-79.
- 454 [17] Davies, C., Pozzo., M., Gubbins D., Alfè, D., 2015. Constraints from ma-
455 terial properties on the dynamics and evolution of Earth's core. *Nature*
456 *Geoscience* 8, 678-685.
- 457 [18] Davies, C., Pozzo., M., Gubbins D., Alfè, D., 2020. Transfer of oxygen to
458 Earth's core from a long-lived magma ocean. *Earth Planet. Sci. Lett.* 538,
459 116208, 1-11.
- 460 [19] Davies, C., Bono, R.K., Meduri, D.G., Aubert, J., Greenwood, S., Big-
461 gin, A.J., 2022. Dynamo constraints on the long-term evolution of Earth's
462 magnetic field strength. *Geophys. J. Int.* 228, 316-336.

- 463 [20] de Koker, N., Steinle-Neumann, G., Vlček, V., 2012. Electrical resistivity
464 and thermal conductivity of liquid Fe alloys at high P and T, and heat flux
465 in Earth's core. *Proc. Natl. Acad. Sci.* 109, 4070-3.
- 466 [21] Desjarlais, M.P., Kress, J.D., Collins, L.A., 2002. Electrical conductivity for
467 warm, dense aluminum plasmas and liquids. *Phys. Rev. E* 66, 025401(R),
468 1-4.
- 469 [22] Driscoll, P., Bercovici, D., 2014. On the thermal and magnetic histories of
470 Earth and Venus: Influences of melting, radioactivity, and conductivity.
471 *Phys. Earth Planet. Int.* 236, 3651.
- 472 [23] Daniel A. Frost, Margaret S. Avery, Bruce A. Buffett, Bethany A.
473 Chidester, Jie Deng, Susannah M. Dorfman, Zhi Li, Lijun Liu, Mingda
474 Lv, Joshua F. Martin, 2022. Multidisciplinary constraints on the thermal-
475 chemical boundary between Earth's core and mantle. *Geochem. Geophys.*
476 *Geosyst.*, doi: 10.1029/2021GC009764.
- 477 [24] Gomi, H., Ohta, K., Hirose, K., Labrosse, S., Caracas, R., Vestraete, M.J.,
478 Hernlund, J.W., 2013. The high conductivity of iron and thermal evolution
479 of the Earth's core. *Phys. Earth Planet. Int.* 224, 88-103.
- 480 [25] Gomi, H., Hirose, K., Akai, H., Fei, Y., 2016. Electrical resistivity of sub-
481stitutionally disordered hcp FeSi and FeNi alloys: chemically-induced re-
482sistivity saturation in the Earth's core. *Earth Planet. Sci. Lett.* 451, 5161.
- 483 [26] Greenwood, D.A., 1958. The Boltzmann equation in the theory of electrical
484 conduction in metals. *Proc. Phys. Soc.* 71, 585-596.
- 485 [27] Gubbins, D., Alfè, D., Masters, G., Price, G.D., Gillan, M.J., 2003. Can
486 the Earth's dynamo run on heat alone? *Geophys. J. Int.* 155, 609622.
- 487 [28] Helffrich, G., Kaneshima, S., 2010. Outer-core compositional stratification
488 from observed core wave speed profiles. *Nature* 468, 807810.

- 489 [29] Hausoel, A., Karolak, M., Şaşlıoğlu, E., Lichtenstein, A., Held, K., Katanin,
490 A., Toschi, A., Sangiovanni, G., 2017. Local magnetic moments in iron and
491 nickel at ambient and Earth's core conditions. *Nat. Commun.* 8, 16062, 1-9.
- 492 [30] Hirose, K., Morard, G., Sinmyo, R., Umemoto, K., Hernlund, J., Helffrich,
493 G., Labrosse, S., 2017. Crystallization of silicon dioxide and compositional
494 evolution of the Earth's core. *Nature* 543, 99-102.
- 495 [31] Hsieh, W.-P., Goncharov, A.F., Labrosse, S., Holtgrewe, N., Lobanov, S.S.,
496 Chuvashova, I., Deschamps, F., Lin, J.-F., 2020. Low thermal conductivity
497 of iron-silicon alloys at Earth's core conditions with implications for the
498 geodynamo. *Nat. Commun.* 11 (1), 1-7.
- 499 [32] Inoue, H., Suehiro, S., Ohta, K., Hirose, K., Ohishi, Y., 2020. Resistivity
500 saturation of hcp Fe-Si alloys in an internally heated diamond anvil cell:
501 A key to assessing the Earth's core conductivity. *Earth Planet. Sci. Lett.*
502 543, 116357, 1-8.
- 503 [33] Ioffe, A.F., Regel, A.R., 1960. Non-crystalline, amorphous and liquid elec-
504 tronic semiconductors. *Prog. Semicond.* 4, 237-291.
- 505 [34] Konôpková, Z., McWilliams, R., Gómez-Pérez, N., Goncharov, A., 2016.
506 Direct measurement of thermal conductivity in solid iron at planetary core
507 conditions. *Nature* 534, 99-101.
- 508 [35] Kresse, G., Furthmüller, J., 1996. Efficiency of ab-initio total energy calcu-
509 lations for metals and semiconductors using a plane-wave basis set. *Comp.*
510 *Mater. Sci.* 6, 15-50.
- 511 [36] Kresse, G., Joubert, D., 1999. From ultrasoft pseudopotentials to the pro-
512 jector augmented-wave method. *Phys. Rev. B* 59, 1758-1775.
- 513 [37] Kubo, R., 1957. Statistical-mechanical theory of irreversible processes. I
514 General theory and simple applications to magnetic and conduction prob-
515 lems. *J. Phys. Soc. Jpn.* 12, 570-586.

- 516 [38] Labrosse, S., Poirier, J.-P., Le Moeul, J.-L., 2001. The age of the inner core.
517 Earth Planet. Sci. Lett. 190, 111-123.
- 518 [39] Labrosse, S., 2015. Thermal evolution of the core with a high thermal
519 conductivity. Phys. Earth Planet. Int. 247, 36-55.
- 520 [40] Landeau, M., Aubert, J., Olson, P., 2017. The signature of inner-core nu-
521 cleation on the geodynamo. Earth Planet. Sci. Lett. 465, 193204.
- 522 [41] Masters, G., Gubbins, D., 2003. On the resolution of density within the
523 Earth. Phys. Earth Planet. Int. 140, 159167.
- 524 [42] Mittal, T., Knezek, N., Arveson, S.M., McGuire, C.P., Williams, C.D.,
525 Jones, T.D., Li, J., 2020. Precipitation of multiple light elements to power
526 Earth's early dynamo. Earth Planet. Sci. Lett. 532, 116030, 1-13.
- 527 [43] Nimmo, F., 2015. Thermal and compositional evolution of the core. In:
528 Schubert, G., (Ed.), Treatise on Geophysics, vol. 9. Elsevier, Amsterdam,
529 pp. 201-219.
- 530 [44] Nimmo, F., Alfè, D., 2007. Properties and evolution of the Earth's core
531 and geodynamo. In: Sammons, P.R., Thompson, J.M.T. (Eds.), Advances
532 in Earth Science: From Earthquakes to Global Warming (Royal Society
533 Series on Advances in Science. Imperial College Press, pp. 167-210.
- 534 [45] Nosé, S., 1984. A molecular dynamics method for simulations in the canon-
535 ical ensemble. Molec. Phys. 52, 255-268; A unified formulation of the con-
536 stant temperature molecular dynamics methods. J. Chem. Phys. 81, 511-
537 519.
- 538 [46] Ohta, K., Kuwayama, Y., Shimizu, K., Yagi, T., Hirose, K., Ohishi, Y.,
539 2014. Measurements of electrical and thermal conductivity of iron under
540 Earth's core conditions. AGU abstract MR21B-06, AGU Fall Meeting, S.
541 Francisco, 15-19 December.

- 542 [47] Ohta, K., Suehiro, S., Hirose, K., Ohishi, Y., 2015. The electrical resistiv-
543 ity of iron alloys at Earth's core conditions. Goldschmidt Conference 2015
544 abstract, A2326, Prague, Czech Republic, 16-21 August.
- 545 [48] Ohta, K., Kuwayama, Y., Hirose, K., Shimizu, K., Ohishi, Y., 2016. Ex-
546 perimental determination of the electrical resistivity of iron at Earth's core
547 conditions. *Nature* 534, 95-98.
- 548 [49] O'Rourke, J.G., Stevenson, D.J., 2016. Powering Earth's dynamo with
549 magnesium precipitation from the core. *Nature* 529, 387-389.
- 550 [50] Pouvroskii, L.V., Mravlje, J., Georges, A., Simak, S.I., Abrikosov, I.A.,
551 2017. Electron-electron scattering and thermal conductivity of ϵ iron at
552 Earth's core conditions. *New J. Phys.* 19, 073022, 1-9.
- 553 [51] Pourovskii, L., Mravlje, J., Pozzo, M., Alfè, D., 2020. Electronic correla-
554 tions and transport in iron at earth's core conditions. *Nat. Commun.* 11
555 (1), 1-8.
- 556 [52] Pozzo, M., Desjarlais, M.P., Alfè, D., 2011. Electrical and thermal conduc-
557 tivity of liquid sodium from first-principles calculations. *Phys. Rev. B* 84,
558 054203, 1-7.
- 559 [53] Pozzo, M., Davies, C., Gubbins, D., Alfè, D., 2012. Thermal and electrical
560 conductivity of iron at Earth's core conditions. *Nature* 485, 355-358.
- 561 [54] Pozzo, M., Davies, C., Gubbins, D., Alfè, D., 2013. Transport properties for
562 liquid silicon-oxygen-iron mixtures at Earth's core conditions. *Phys. Rev.*
563 *B* 87, 014110-10.
- 564 [55] Pozzo, M., Davies, C., Gubbins, D., Alfè, D., 2014. Thermal and electrical
565 conductivity of solid iron and iron-silicon mixtures at Earth's core condi-
566 tions. *Earth Planet. Sci. Lett.* 393, 159-164.
- 567 [56] Pozzo, M., Alfè, D., 2016a. Saturation of electrical resistivity of solid iron
568 at earth's core conditions. *SpringerPlus* 5 (1), 1-6.

- 569 [57] Pozzo, M., Alfè, D., 2016b. Electrical resistivity saturation of solid iron at
570 Earth's core conditions from density functional theory. In AGU Abstract
571 DI13A-2356, AGU Fall Meeting (San Fransisco, CA).
- 572 [58] Secco, R. A., 2017. Thermal conductivity and Seebeck coefficient of Fe and
573 Fe-Si alloys: Implications for variable Lorenz number. *Phys. Earth Planet.*
574 *Int.* 265, 23-34.
- 575 [59] Sha, X., Cohen, R.E., 2011. First-principles studies of electrical resistivity
576 of iron under pressure. *J. Phys.: Condens. Matter* 23, 075401, 1-5.
- 577 [60] Silber, R.E., Secco, R.A., Yong, W., Littleton, J.A.H., 2019. Heat flow
578 in Earth's core from invariant electrical resistivity of Fe-Si on the melting
579 boundary to 9 GPa: do light elements matter? *J. Geophys. Res. Solid*
580 *Earth* 124, 5521-5543.
- 581 [61] Stacey, F.D., Anderson, O.L., 2001. Electrical and thermal conductivities of
582 Fe-Ni-Si alloy under core conditions. *Phys. Earth Planet. Int.* 124, 153-162.
- 583 [62] Stacey, F.D., Loper, D.E., 2007. A revised estimate of the conductivity of
584 iron alloy at high pressure and implications for the core energy balance.
585 *Phys. Earth Planet. Int.* 161, 13-18.
- 586 [63] Tarduno, J. et al., 2010. Geodynamo, solar wind, and magnetopause 3.4 to
587 3.45 billion years ago. *Science* 327, 12381240.
- 588 [64] Wang, Y., Perdew, J.P., 1991. Correlation hole of the spin-polarized elec-
589 tron gas, with exact small-wave-vector and high-density scaling. *Phys. Rev.*
590 *B* 44, 13298-13307; Perdew, J.P., Chevary, J.A., Vosko, S.H., Jackson, K.A.,
591 Pederson, M.R., Singh, D.J., Fiolhais, C., 1992. Atoms, molecules, solids,
592 and surfaces: Applications of the generalized gradient approximation for
593 exchange and correlation. *Phys. Rev. B* 46, 6671-6687.
- 594 [65] Xiong, Z., Tsuchiya, T., Taniuchi, T., 2018. Ab Initio prediction of potas-
595 sium partitioning into Earth's Core. *J. Geophys. Res.: Solid Earth* 123,
596 6451-6458.

- 597 [66] Xu, J., Zhang, P., Haule, K., Minar, J., Wimmer, S., Ebert, H., Cohen, R.,
598 2018. Thermal conductivity and electrical resistivity of solid iron at Earth's
599 core conditions from first principles. *Phys. Rev. Lett.* 121 (9), 096601, 1-6.
- 600 [67] Zhang, Y., Hou, M., Liu, G., Zhang, C., Prakapenka, V.B., Greenberg,
601 E., Fei, Y., Cohen, R., Lin, J.-F., 2020. Reconciliation of experiments and
602 theory on transport properties of iron and the geodynamo. *Phys. Rev. Lett.*
603 125 (7), 078501, 1-7.